An Accurate Experimental Determination of Effective Strain for Heterogeneous Electronic Packages With Digital Image Correlation Method

Yuling Niu, Van-Lai Pham, Jing Wang, and Seungbae Park

***Abstract*— This paper presents an accurate experimental method to determine the effective strain for the advanced electronic packages with heterogeneous structure or multiple composite layers when the out-of-plane deformation has evident effects on the in-plane strain quantification. The experimental results rely on the 3-D digital image correlation (DIC) technique, a full-field optical measurement method. Several advantages make this technique a perfect choice for characterizing the effective strain for electronic packages, especially for the heterogeneously designed packages that are likely to have large warpage after reflow process. In order to generate the effective strain with the consideration of warpage and thickness effects, an improved data process algorithm for 3-D DIC is introduced to obtain the neutral plane strain. The result was validated analytically and numerically based on the Timoshenko beam theory and finite-element method. The effectiveness and necessity of this paper are demonstrated by applying the results into a practical multilayer package and forecasting the accurate behavior under thermal loading.**

***Index Terms*— Integrated circuit measurements, integrated circuit reliability, measurement techniques, stereo image processing.**

I. Introduction

THE strain of the electronic packages on different layers is an important source for learning their reliability and to decide the effective coefficient of thermal expansion (CTE), which is the most critical parameter for establishing a reliable model [1]. The composite materials are extensively utilized in electronic packaging. To pursue the goal of fabricating the devices that are thin and light, manufacturers have to limit the thickness, which inevitably makes the design unsymmetrical. Furthermore, the novel packages with heterogeneous structure, like the embedded chips in substrate or molding, exaggerate the mismatch of material properties. These issues lead to the out-of-plane deformation when packages are under thermal loading. The out-of-plane deflection (warpage) plays an important role in accurately estimating the effective thermal strain [2]. Several analytical and numerical models point out the effects of the out-of-plane deformation on the in-plane strain determination for bilayer [3], [4] or sandwich structure [5], especially for microelectronic packaging materials [6], [7]. It indicates that researchers noticed the significance of the issue and attempted to reveal the fact with analytical or numerical method [8]. Actually, the composite materials or the heterogeneous designed packages are more complicated than these proposed models. The analytical solutions cannot be used for analyzing designs with irregular geometry with various materials [9]. To illustrate the effective strain, it is more efficient to directly perform the real measurement to determine it [10].

The conventional thermal strain measurement methods can be classified as sensor contact method, such as thermomechanical analyzer (TMA) [11] or strain gauge, and optical fringe method, such as Moiré interferometer [12]. Nowadays, these two methods reached their limits for the more precise and convenient measurement demands. TMA has a strict dimension requirement for samples that should be cut into certain sizes for the test. When it reports the strain versus temperature curve to depict the CTE of the material, it employs one contact sensor on the top of the sample to track the displacement. The strain result cannot be accurate when the sample deforms on the horizontal (out-of-plane) direction or the sensor does not contact the sample properly. The distortion of the sample makes the contact into point-to-surface contact, which loses the contact on the neutral plane. Moreover, the preload applied on the sample may enlarge the bending of the specimen, especially for soft polymers. The out-of-plane deflection (warpage) generates great influences on the determination of the effective strain since the expansion is no longer planar. Moiré interferometer requires specimen preparation of the polished cross-sectional surface, while the black and white fringes are arranged with gray values to interpolate the displacement between each fringe [13]. It epitomizes the low efficiency with which these methods determine strain in one direction for each test.

Regarding these concerns, it is necessary to seek for an accurate experiment method to determine the effective strain for electronic packages with mixed layers. Initially, improved Moiré interferometer developed the transient thermal strain measurement method [14]. Later, 2-D digital image correlation (DIC) was created to learn the surface strain with the arrival of digital image decade [15]. The featured

Manuscript received August 26, 2017; revised November 19, 2017; accepted January 12, 2018. Date of publication February 9, 2018; date of current version April 12, 2018. Recommended for publication by Associate Editor I. C. Ume upon evaluation of reviewers' comments. *(Corresponding author: Yuling Niu.)*

The authors are with the Opto-Mechanics and Physical Reliability Laboratory, State University of New York at Binghamton, Binghamton, NY 13902 USA (e-mail: yniu1@binghamton.edu).

Color versions of one or more of the figures in this paper are available online at http://ieeexplore.ieee.org.

Digital Object Identifier 10.1109/TCPMT.2018.2794505

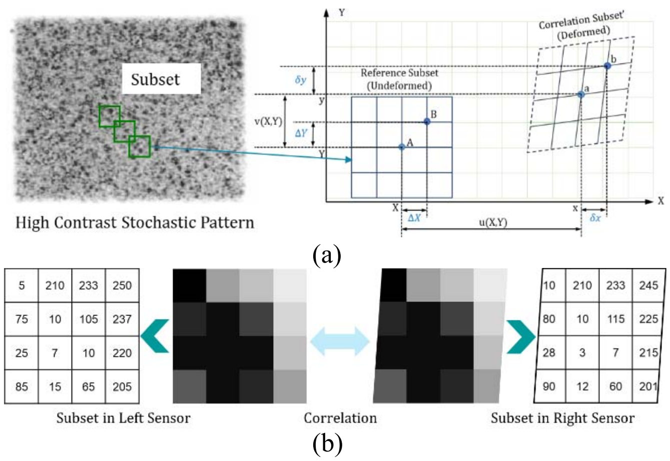

Fig. 1. (a) Division and movement track of 2-D DIC subset. (b) Subset recognition from left and right sensor.

surface is divided into many small subsets and the movement of each subset is recorded [Fig. 1(a)]. It measures the strain in all paths and locations within one test, and directly traces the displacement without interpolation, which improves the test efficiency. Later, 3-D DIC served as an optical and noncontact warpage measurement method and gradually replaced the conventional tools in the electronic packaging area [16]. Two cameras monitor the identical subset to construct gray value matrix for each subset independently. Through the similarity correlation, the outlines of the subset are depicted and the spatial orientation of the subsets is described [Fig. 1(b)] [17]–[20]. It acquires the *in situ* digital images and correlates them to generate surface topography with high measurement sensitivity. Not only for warpage, but also the in-plane deformation can be quantified simultaneously during a 3-D DIC test. It makes 3-D DIC, which possesses the ability of characterizing displacement in all the directions, an ideal solution to determine the effective strain including the effects of out-of-plane deformation.

The out-of-plane rigid body movement effects on 3-D DIC result were discussed in Sutton's study [21], but the out-of-plane deformation cannot be assessed universally. De Almeida *et al.* [22] utilized a mirror to learn the lateral surface deformation, while the cameras focused on the front surface, to reconstruct the volume with 3-D DIC. However, the warpage behavior of electronic packages is quite different from edges to center, which means that the reconstruction according to the lateral surface may be inaccurate. This paper attempts to examine the basic principles to see the current limitations of 3-D DIC in determining the effective strain, because warpage becomes a universal issue for packages and becomes more serious with heterogeneous structures. Aiming to illustrate the neutral plane effective strain of heterogeneous packages and improve the conventional 3-D DIC algorithm, a novel process method was proposed and compared to obtain the accurate result based upon the 3-D DIC data acquisition. With the consideration of shear force influences, the analytical solutions based on the Timoshenko beam theory [23] were derived to validate the experimental results. In the end, the average CTE, derived from the neutral plane strain, was applied to a realistic heterogeneously designed package to solidify the effectiveness and precision of the method.

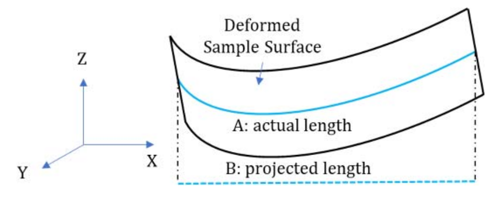

Fig. 2. Schematic of deformed sample with actual section length and projected section length.

II. Surface Topography Determination of 3-D DIC

DIC includes two fundamental functions: image acquisition and correlation. The conventional 2-D DIC captures the projected length (Fig. 2). After taking several image stages in real time, 3-D DIC compares the left and right images, such as the principle of human eye perspective, and correlates the successive image stages as the loading varies. Then, it obtains both in-plane displacement and out-of-plane deformation. The combination of in-plane and out-of-plane information realizes to measure the actual length in Fig. 2. Therefore, it calculates the deformation based on the planar assumption, which means the out-of-plane displacement should be relatively small. So, it remains to be justified when the deflection of the sample reaches the error limit of the 3-D DIC. More specifically, as shown in Fig. 2, it is necessary to ensure that 3-D DIC reports the real strain on the deformed samples surface at different out-of-plane deflection levels.

A. Image Correlation Algorithm

To reveal the dependence of 3-D DIC in-plane coordinate with the out-of-plane information, the image mapping analytical equations [24] are expressed according to the coordinate transformation principle (Fig. 3) as follows:

$$Z_{\text{c\_cam1}} = \frac{f_1 \cdot Z_p \cdot \kappa}{f_1 \cdot \kappa + X_{\text{s\_cam1}} \cos\theta + Y_{\text{s\_cam1}} \cos\phi} \quad (1)$$

$$X_{\text{c\_cam1}} = \frac{X_{\text{s\_cam1}} \cdot Z_p \cdot \kappa}{f_1 \cdot \kappa + X_{\text{s\_cam1}} \cos\theta + Y_{\text{s\_cam1}} \cos\phi} \quad (2)$$

$$Y_{\text{c\_cam1}} = \frac{Y_{\text{s\_cam1}} \cdot Z_p \cdot \kappa}{f_1 \cdot \kappa + X_{\text{s\_cam1}} \cos\theta + Y_{\text{s\_cam1}} \cos\phi} \quad (3)$$

$$Z_p \cdot \kappa = X_{c_{\text{cam1}}} \cos\theta + Y_{c_{\text{cam1}}} \cos\phi + Z_{c_{\text{cam1}}} \cdot \kappa \quad (4)$$

where $\kappa = (1 - (\cos\theta)^2 - (\cos\phi)^2)^{1/2}$.

Here the subscript of "c_cam" means that the camera coordinate system, while "s_cam" indicates the sensor coordinate system. As the algorithm performs the image correlation process, the image information from sensor transforms to camera coordinate to utilize the calibrated camera system information. θ and φ represent the angular direction from normal vector $\vec{n}$ to subset location and Z_p stands for the norm of the vector. f_1 is the focal length. All these parameters are directly obtained from the calibration process. Equations (2) and (3) show that the determination of in-plane coordinate

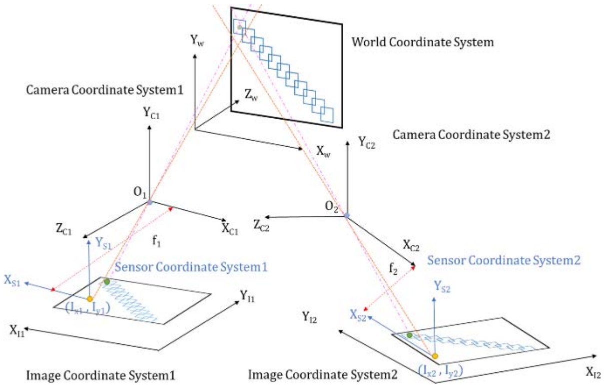

Fig. 3. Transformation algorithm from world and camera coordinate to sensor and image coordinate.

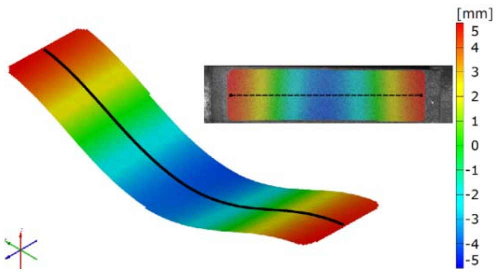

Fig. 4. Warpage contour of deflected paper.

requires the out-of-plane distance Z_p, but it assists only to decide the perspective virtual plane on the basis of similar triangles. At the same time, the out-of-plane displacement is highly dependent on the judgment of X and Y coordinates. With the analysis of the coordinate determination, it explains how the image correlation defines and recognizes the position of each subset without indicating the error limit of out-of-plane deformation. The out-of-plane deformation restriction is related to the image correlation deviation. To understand the out-of-plane displacement limit of 3-D DIC, an experiment was designed to illustrate the error range, and the subset factor was studied as well.

B. Length Error at Different Deflections

A piece of paper and thin copper foil, without expansion or shrinkage, were measured separately by 3-D DIC. A standard section length was drawn on each sample to be the reference for strain error, which is 59.600 mm for paper and 60 mm for thin copper. When the specimen was deflected (Fig. 4), or warped at different deflections, the length of the identical section was reported with different subset sizes.

The subset size of 3-D DIC is similar to model mesh density. It means a unit that includes several pixels to be correlated. In Fig. 1(b), the subset size is 4×4 pixels. These subsets are the basic calculation unit, which are assumed as a rigid plane. The objective of image correlation is to recognize all the positions of the subset and connect them with smooth surface. The larger the subset size, the lower will be the data density. Deflection represents the out-of-plane deformation of the specimen, which is the critical reliability issue for

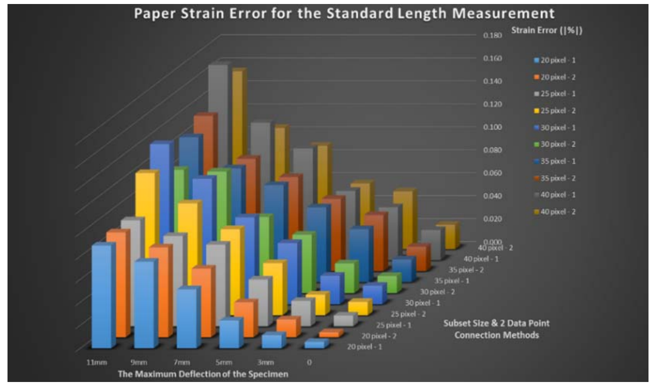

Fig. 5. Strain errors for the paper specimen with different warping deflections and subset sizes.

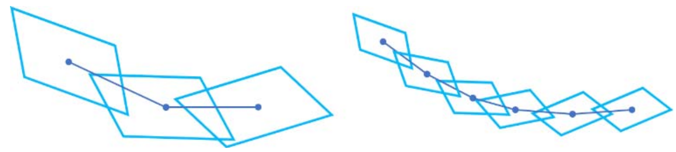

Fig. 6. Schematic of connection with two different subset sizes.

electronic packages. The z-direction movement is the principal challenge to achieve the accurate length information.

Fig. 5 shows the strain errors for different subset sizes and deflections, while the copper foil result can be found in Appendix A, which is similar result with Fig. 5. At the same subset size and deflection level, "−1" and "−2" means that the results calculated by two 3-D DIC systems. The strain errors of two 3-D DIC programs are different due to the variance of correlation deviation tolerance, but the trends of the strain error are consistent as the subset size and deflection increase. It is obvious that 3-D DIC provides quite an accurate result, lower than 0.04%, when the deflection is small, less than 3 mm. However, as the deflection increases, similar to warpage occurrence of packages under thermal loading, the section length turns inaccurate and the error percentage increases. Though the strain error shows 0.20% maximum, the section length is within a reasonable range so that it guarantees that the measured length is the actual length, not projected length. It indicates that 3-D DIC adds the out-of-plane deformation effects to calculate effective strain, but it loses accuracy as the deflection increases. The fundamental correlation algorithm is based on the planar assumption, and makes adjustments for out-of-plane deformation. When the ratio of warpage to sample length is large, such as 11 to 60 mm in Fig. 5, about 19% deflection to the length, the error of strain calculation is introduced and exaggerated. Based on statistical result that 3-mm deflection keeps the error to less than 0.04% for 60 mm length, it can be concluded that the strain result is accurate when the deflection to length ratio is lower than 1:20.

The subset size affects the accuracy of strain measurement as well. It is noticed that the error changes as the subset size increases, when the specimen is bent. The large subset size results in the low data point density (Fig. 6). When the system

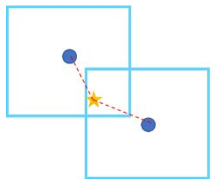

Fig. 7. Schematic of the data point approximation to the target point with different subset sizes.

tries to combine two marked points to report distance, the large subset size, which means a low data point density, will make it difficult to approximate the closest points to the target points. Fig. 7 shows the schematic of the subset approximation method. If the star is the target point, the two adjacent subsets can be adopted to measure the distance or strain, while the smaller subset size can reduce the error. A quick conclusion is that the accurate strain calculation requests small subset size to minimize the error. However, this output is contrary to the subset selection rules, which were constructed with the standard of image correlation deviation [25]. The previous works proved that the large subset can reduce the image process standard deviation because the large subset means that more pixels are correlated and more information is collected to verify the subset location. In this dilemma, either the correlation error or the strain calculation error has to be sacrificed. This paper again demonstrates the subset size selection perplexity, and Niu *et al.* [26] recommend a compromise of the two types of errors and seek the balance between them. Regarding the particular application area, the empirical equations can assist in choosing the optimal subset size. Meanwhile, Hassan *et al.* [27] provided the dynamic subset selection method. This topic can be further discussed and studied in the future. In the rest of this work, the subset size is maintained at a low level, around 20 to 30 pixels, to achieve high subset density.

The increasing tendency of strain errors from two DIC systems is consistent as the deflection increases. The evident bias that should be noticed is the data points are connected directly with straight lines. Depending on the data density, the actual curved surface would be different to the calculated length. To summarize briefly, DIC method is able to combine the out-of-plane and in-plane displacements together and export the actual length, on the threshold that the warpage does not exceed 5% of package dimension. The approximation of subset point to target point and the subset connection may have some initial biases for accurate strain determination.

III. Accurate Strain Determination on Neutral Plane

A. Warpage and Thickness Effects

With confidence of the confirmed DIC technique, several experiments were conducted to quantify the thermal strain of the packaging components, which laid a solid foundation for constructing the numerical models. However, a test result of the printed circuited board assembly (PCBA), which has heterogeneous components on it, reminds us the effective strain should be on the neutral plane. The PCBA is $356\times356\times7$ mm^3 with two 75×55 mm^2 packages on the bottom surface. The PCB has 20 layers of copper circuits, prepreg materials and solder mask. Fig. 8(a) shows the warpage distribution of the PCBA at 250 °C and the strain was measured along y-direction. Fig. 8(b) shows the surface strain versus temperature plot. The interesting phenomenon is that the high-temperature zone (150 °C to 250 °C) displays the negative thermal expansion, which seems it has shrunk. Its warpage is shown in Table I. The 7-mm-thick sample has 5 mm relative deformation from room temperature to 250 °C due to its heterogeneous layers and attached components. As the warpage increases, the surface strain shows lower than the realistic value. From 25 °C to 150 °C, the surface strain is kept lower than the reality. After 150 °C, the top surface generates the relative shrinkage as compared to it at 150 °C because the evident warpage jumped up from −2.185 to −3.446 mm at 175 °C, which doubled the relative warpage from room temperature to 150 °C (−0.994 to −2.185 mm).

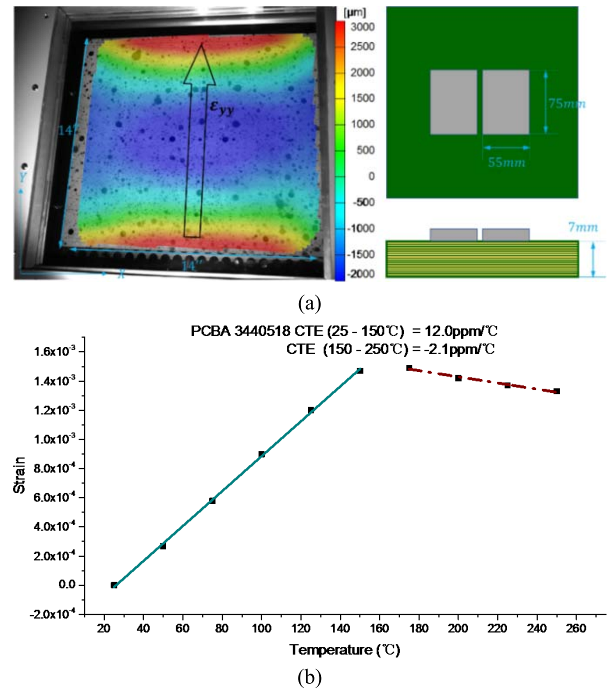

Fig. 8. (a) PCBA structure and dimensional specs. (b) PCBA top surface strain versus temperature plot.

TABLE I
Maximum Warpage of the PCBA

Temperature (°C)	25	50	75	100	125
Warpage (mm)	-0.99	-1.00	-1.11	-1.45	-1.91
Temperature (°C)	150	175	200	225	250
Warpage (mm)	-2.18	-3.45	-4.37	-5.08	-5.83

In this case, though the 3-D DIC still depicts the accurate surface strain, the neutral plane strain can be far away from the top surface strain (Fig. 9). It is the scenario wherein the thickness of the specimen exaggerates the differences between surface strain and the neutral plane strain, like the schematic

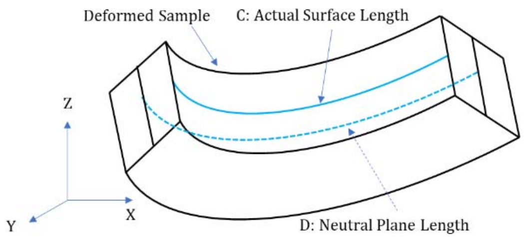

Fig. 9. Schematic of the measured surface length versus neutral plane length for the deformed sample with certain thickness.

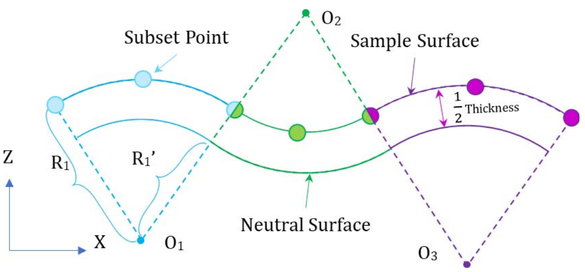

Fig. 10. Schematic of three-point common curvature method to connect the data points and calculate the neutral plane strain.

in Fig. 9, when the warpage shows impact on thick sample to generate an unreal result. In the early age of packaging area, the thickness and warpage of packages were small so that the surface strain could be approximated as the neutral plane strain. Due to the high density and integration request from the customers, the packages are built stereoscopically, and the warpage becomes a critical reliability problem. The trend of the electronic packages moves to the 2.5-D or 3-D package and keeps increasing the thickness. During the development, the complicated structures aggravate the CTE mismatch among the layers. The heterogeneously designed packages generate more warpage during assembly process. The effective strain determination demands to be resolved on neutral plane.

B. 3-D DIC Solution

The cross-sectional surface of specimen can be a way to learn the neutral plane strain, but there remain potential errors when we manually count the fringe lines. To learn the strain on different directions, adequate surfaces must be severed in each direction to perform the measurements. DIC generates the full-field surface strain and warpage at the same time. Therefore, it is more efficient to improve it to describe the full-field neutral plane strain. In this regard, this paper proposes the method to compensate the warpage influences on thickness.

According to the features of 3-D DIC data, a novel data process method is proposed. 3-D DIC can export all the subset locations on sample surface. The accuracy of surface data was validated in Section II. Instead of connecting points with straight lines, this paper investigates to combine every three points by evaluating their common curvature R_1, curve length L, and the curvature center O_1 in Fig. 10. The three points share the identical radius from (5), as shown at the bottom of the next page, and lay on the curve, where (x_1, z_1), (x_2, z_2), and (x_3, z_3) are three points on the xy coordinate, and $k_1 = -((x_1 - x_2)/(z_1 - z_2)), k_2 = -((x_3 - x_2)/(z_3 - z_2))$. Depending on the strain direction, the coordinate can be transformed to any projected plane along the strain direction to convert the 3-D coordinate to a 2-D coordinate.

Compared to traditional data point connection method, this method has several advantages. On one hand, the straight-line connection definitely shortens the actual surface strain, because it simplifies a smooth curve into some straight lines. Referring to the result in Section II, the error range is acceptable, but it permanently indicates the initial bias. The three-point curve, which relies on the formation of three-point common curvature, can approach the actual curve length. On the other hand, the three-point common curvature helps to recalculate the neutral plane strain readily. Based on the shared curvature center, the curve length can be calculated by subtracting half of the thickness to obtain the new radius R_1' in (6), as shown at the bottom of the next page. Depending on the input of the sample thickness, the effective neutral plane strain can be achieved easily. A quick note about the schematic of Fig. 10 is that it shows the xy plane while the subset locations are 3-D coordinates. Due to the strain calculation along the direction, it is simple to project all the xy coordinates into the new x' coordinate along a section. Then the strain calculation is based on the new $x'z$ plane.

C. Effectiveness of 3-D DIC Strain Determination

In order to demonstrate the usefulness of 3-D DIC neutral plane strain determination method, a series of verification tests was performed. For verification tests, metal blocks were bonded to the firm wall to mimic the cantilever beam (Fig. 11). The loading P was applied at the end of the beam to generate bending moment to imitate the warpage occurrence. As loading P increases, the deflection worsens. At the same time, the 3-D DIC system captures the bending process and reports the elongation of top surface. The data points were connected by three-point curvature method to obtain the neutral plane strain. Based on the subset data on the top surface, the proposed method computes the neutral plane strain with the input of sample thickness. Numerical models and analytical solutions were established to verify the deflection at the point H, elongation of top surface, and neutral plane length with different loadings, sample thickness, and specimen. To avoid the mesh density effects on stress singularity for multilayered structures at the free end [9], the test sample was uniform metal block and the beam elongation strain was utilized as the standard reference.

The analytical solutions relied on the Timoshenko beam theory [28], which includes the effect of shearing force on the deflected beam. At fixed end O, the condition constraint is $(\partial u/\partial z)_{x=0,z=0} = 0$, instead of $(\partial w/\partial x)_{x=0,z=0} = 0$, which is the constraint condition for Euler–Bernoulli beam [29], [30]. Then, the horizontal displacement u and deflection w on any point of the cantilever beam are as follows:

$$\begin{cases} u = \dfrac{Pzx^2}{2EI} - \dfrac{Plzx}{EI} + \dfrac{\nu P z^3}{6EI} - \dfrac{Pz^3}{6GI} & (8) \\ w = -\dfrac{Px^3}{6EI} + \dfrac{Plx^2}{2EI} + \left(\dfrac{Pt^2}{2GI} - \dfrac{\nu P z^2}{2EI}\right)x + \dfrac{\nu P l z^2}{2EI} & (9) \end{cases}$$

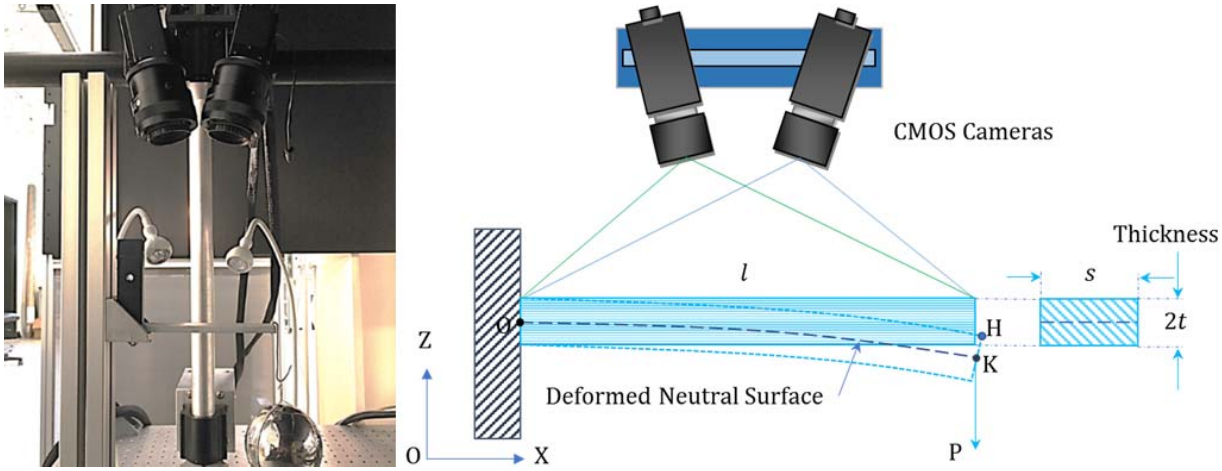

Fig. 11. Schematic and experimental setup for validating the neutral plane strain calculation method.

where E is the material Young's modulus, and G is the modulus of rigidity. ν stands for Poisson's ratio and the moment of inertia is $I = (2/3) \cdot s \cdot t^3$. The derivation process is listed in Appendix B. Through geometric information, the top surface and neutral plane displacement can be written as follows:

$$u_{(z=t)} = \frac{Pt}{2EI}x^2 - \frac{Plt}{EI}x + \frac{\nu Pt^3}{6EI} - \frac{Pt^3}{6GI} \tag{10}$$

$$w_{(z=t)} = \frac{Pl}{2EI}x^2 - \frac{P}{6EI}x^3 + \left(\frac{Pt^2}{2GI} - \frac{\nu Pt^2}{2EI}\right)x + \frac{\nu Plt^2}{2EI} \tag{11}$$

$$u_{(z=0)} = 0 \tag{12}$$

$$w_{(z=0)} = -\frac{P}{6EI}x^3 + \frac{Pl}{2EI}x^2 + \frac{Pt^2}{2GI}x. \tag{13}$$

With the displacement, the total length after deformation

$$l_{\text{surface}} = \int_0^l \sqrt{\left(1 - \frac{Plt}{EI} + \frac{Ptx}{EI}\right)^2 + \left(\frac{Plx}{EI} - \frac{Px^2}{2EI} + \frac{Pt^2}{2GI} - \frac{\nu Pt^2}{2EI}\right)^2}\, dx \tag{14}$$

$$l_{\text{neutral\_plane}} = \int_0^l \sqrt{1 + \left(\frac{Plx}{EI} - \frac{Px^2}{2EI} + \frac{Pt^2}{2GI}\right)^2}\, dx. \tag{15}$$

The analytical solutions are based on assumptions of beam deformation conditions. It works as the reference for experiment and simulation results. The numerical models were built [Fig. 12(a)] with two elements: 1) Beam 189, which follows the Timoshenko beam theory, and 2) the Solid 185, which is closer to actual condition. The results of the maximum beam deflection, the top surface elongation strain, and neutral plane length together with the 3-D DIC experiment output [Fig. 12(b)] are listed in Tables II–IV.

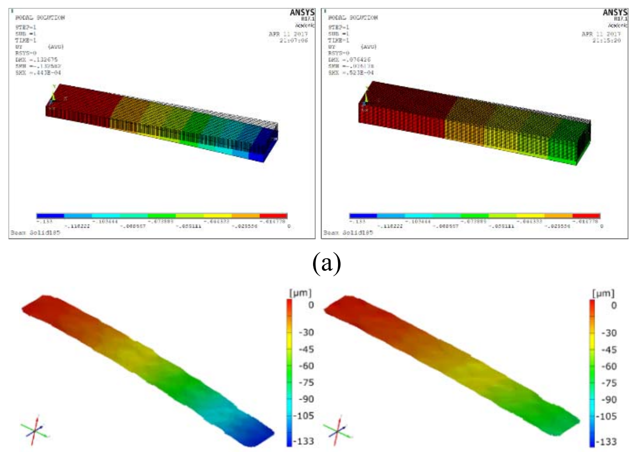

Fig. 12. (a) Cantilever beam model of Beam 189 and Solid 185. (b) Experimental beam deflection of the 3-D DIC.

Table II presents the top surface elongation strain when the loading was applied to specimen. Solid 185 element results are treated as the standard to compare to others. The 6011 Aluminum is set with the Young's modulus 68.9 Gpa and Poisson's ratio 0.35, while the 110 Copper utilizes 115 Gpa

$$R_1 = \frac{\sqrt{[z_1 - z_3 + k_1(x_1 - x_2) + k_2(x_2 + x_3 - 2x_1)]^2 + [k_1(z_2 - 2z_1 + z_3) + k_2(z_1 - z_2) + k_1k_2(x_1 - x_3)]^2}}{2|k_1 - k_2|} \tag{5}$$

$$R_1' = R_1 - \frac{1}{2}\text{Thickness} \tag{6}$$

$$L = R_1' \cdot \sin^{-1} \frac{\sqrt{(x_1 - x_3)^2 + (y_1 - y_3)^2 + (z_1 - z_3)^2}}{2R_1} \tag{7}$$

TABLE II

SURFACE STRAIN WITH DIFFERENT MATERIALS AND LOADINGS FROM ANALYTICAL, NUMERICAL, AND EXPERIMENTAL RESULTS

Sample (mm)	Surface Strain / Loading	S185 (ppm)	B189 (ppm)	Analytical (ppm)	3D DIC (ppm)
6.35 Al	2.5lb	64.30	62.79	64.30	59.76
	4.2lb	108.18	105.15	109.69	100.61
	6.5lb	167.18	163.40	174.75	161.89
6.35 Cu	2.5lb	38.05	37.29	38.05	33.49
	4.2lb	64.69	60.88	63.93	63.93
	6.5lb	99.70	97.41	101.22	102.74
12.7 Al	2.5lb	18.17	15.90	15.90	14.39
	4.2lb	30.29	26.50	26.50	24.23
	6.5lb	46.95	40.89	40.89	41.65
12.7 Cu	2.5lb	10.67	9.14	9.14	8.38
	4.2lb	18.28	16.00	16.00	13.71
	6.5lb	28.19	24.38	24.38	30.47

TABLE III

DEFLECTION AT POINT H WITH DIFFERENT MATERIALS AND LOADINGS FROM ANALYTICAL, NUMERICAL, AND EXPERIMENTAL RESULTS

Sample (mm)	Deflection / Loading	S185 (μm)	B189 (μm)	Analytical (μm)	3D DIC (μm)
6.35 Al	2.5lb	225.14	229.59	229.70	224.23
	4.2lb	378.27	385.71	385.89	375.84
	6.5lb	585.47	596.92	597.21	595.81
6.35 Cu	2.5lb	132.58	135.09	135.16	135.02
	4.2lb	222.75	226.96	227.06	226.11
	6.5lb	344.76	351.24	351.41	348.90
12.7 Al	2.5lb	29.30	28.86	28.82	29.22
	4.2lb	49.22	48.48	48.42	48.64
	6.5lb	76.18	75.03	74.94	75.28
12.7 Cu	2.5lb	17.26	16.98	16.96	16.90
	4.2lb	29.00	28.53	28.49	28.42
	6.5lb	44.88	44.15	44.10	45.50

and 0.343, respectively. The Beam 189 and analytical solution can be a perfect approximation when the beam deflection is small (Table III). As the deformation increases, the nonlinear elastic behavior begins to show the influences on the validation results. Similarly, the ignorance of high-order items for strain derivation leads to the bias when the effects of out-of-plane deformation cannot be ignored. Given that the variance is limited in 7 ppm for 600-μm deflection, the Timoshenko beam still can be an accurate and fast solution.

In Table III, the similitude of the four columns proves the effectiveness of analytical and the 3-D DIC results. The subset information is mapped with three-point common curvature method (Fig. 10). Compared to the Timoshenko beam solution, 3-D DIC is even closer to the Solid 185 results. When the deflection is large, the top surface elongation of 3-D DIC in Table II approaches to the standard as well. The error is within 8 ppm, which matches the previous error study in Section II. To seek the final goal of the neutral plane strain, the results of neutral plane length from analytical solution and 3-D DIC common curvature method are displayed in Table IV. It should be illustrated that the finite-element models are based on the

TABLE IV

NEUTRAL PLANE LENGTH WITH DIFFERENT MATERIALS AND LOADINGS FROM ANALYTICAL, NUMERICAL, AND EXPERIMENTAL RESULTS

Sample (mm)	Neutral / Loading	Original Length (mm)	Analytical (mm)	3D DIC (mm)
6.35 Al	2.5lb	132.1926	132.1928	132.1923
	4.2lb		132.1933	132.1921
	6.5lb		132.1942	132.1921
6.35 Cu	2.5lb	131.3991	131.3992	131.3989
	4.2lb		131.3993	131.3996
	6.5lb		131.3997	131.4001
12.7 Al	2.5lb	132.0564	132.0564	132.0557
	4.2lb		132.0564	132.0566
	6.5lb		132.0564	132.0562
12.7 Cu	2.5lb	131.2610	131.2610	131.2607
	4.2lb		131.2610	131.2603
	6.5lb		131.2610	131.2614

assumption that the neutral plane is the geometric center. Both Solid 185 and Beam 189 must maintain the neutral plane identical to the original length consistently. On the contrary, the analytical equations (12) and (13) indicate that the neutral plane do not move along the x-direction, because the initial purpose of Timoshenko beam theory aims to predict the deflection of the beam. The analytical solutions with 12.7 mm thickness are exactly the same as the original length. As the thickness decreases and the deflection increases, the analytical solution loses the accuracy up to 14 μm with 597.21 μm z-direction bending. The improper boundary conditions and the ignorance of strain derivation can be the root causes of this inaccuracy.

According to Tables II and III, it can be summarized that the analytical solution can be a good prediction for beam deflection, but will be inaccurate on the neutral plane when the deflection is large. Meanwhile, the neutral plane length on the basis of 3-D DIC data points matches the original length within plus or minus 8 μm for the 130 mm total length. Instead of reporting the top surface elongation in Table IV, the three-point common curvature method generates a relatively stable value on neutral plane as the loading increases. For different samples, the adjustable thickness readily tunes the radius to recalculate the neutral plane. The advantage of the 3-D DIC measurement is that the error on neutral plane strain is not affected by the deflection, when the warpage is limited within 5% of the length, concluded from Section II. Through two numerical models and one analytical solution, the accuracy and the usefulness of three-point common curvature method for neutral plane strain determination method are verified. The demonstration of method effectiveness lays a solid foundation for studying the accurate behaviors of heterogeneously designed packages.

Sometimes, the neutral plane strain is not sensitive to the external mechanical load, as illustrated by Table IV, because the specimen is not expanded or shrunk. For the sake of convenience, the validation test is only designed with the mechanical load to demonstrate the method accuracy. For heterogeneous electronic packages or composite materials, the principal failure issues come from the thermal loadings.

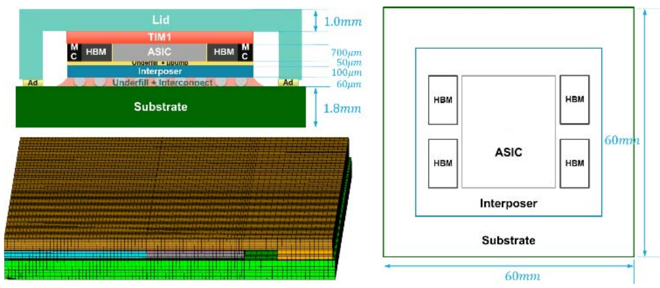

Fig. 13. Cross-sectional surface schematic, floor plan, and quarter symmetric model of a heterogeneous package.

TABLE V

WARPAGE FROM 3-D DIC AND MODEL WITH THE SURFACE CTE 15.9 ppm/°C AND NEUTRAL PLANE CTE 15.4 ppm/°C

Method / Warpage	3D DIC	Surface CTE	Variance	Neutral CTE	Variance
25°C (μm)	-189.5	-211.4	-11.6%	-196.5	-3.7%
50°C (μm)	-149.6	-162.8	-8.8%	-151.3	-1.1%
75°C (μm)	-103.0	-114.4	-11.1%	-106.3	-3.2%
100°C (μm)	-59.4	-66.3	-11.6%	-61.6	-3.7%
125°C (μm)	-14.2	-18.4	-29.6%	-17.0	-19.7%
150°C (μm)	24.3	20.4	-16.0%	18.5	-23.8%
175°C (μm)	41.6	48.0	15.4%	43.2	3.8%
200°C (μm)	76.9	73.0	-5.0%	65.4	-14.9%

These packages inevitable induce warpage when they expand or shrink with thermal loading due to the unsymmetrical structure. In this case, the neutral plane strain is highly related to the external thermal loading. This paper aimed to resolve the errors that are generated by using surface strain to represent the neutral plane strain. When the actual measurements focus on the electronic packages with thermal loading, the neutral plane strain must change and highly dependent on the loadings.

IV. ACCURATE NEUTRAL PLANE STRAIN APPLICATION

Section III displays the strain variance between neutral plane and top surface and also the effectiveness of 3-D DIC to report the accurate neutral plane strain. For the application of heterogeneously designed packages, the accurate strain on neutral plane becomes the key factor in establishing a reliable model. During the investigation of a 60 × 60 mm^2 2.5-D package (Fig. 13), the test vehicle was measured on the substrate.

The package consists of substrate, interposer, ASIC and HBM dies, lid and relevant interconnections, and interfacial materials. The model defines the whole substrate with effective modulus and CTE. Its diagonal warpage and CTE, which relies on the calculation of substrate surface strain under the thermal loading, are generated [Fig. 14(a) and (b)]. The package has 270-μm warpage from room temperature to 200 °C [Fig. 14(b)]. According to the basic material properties, a quarter symmetric numerical model was built (Fig. 13).

When CTE, measured on substrate surface, 15.9 ppm/°C, was input into the finite-element model, the warpage was exported as the solid lines in Fig. 15. The warpage trend and the stress-free temperature are consistent with the 3-D DIC

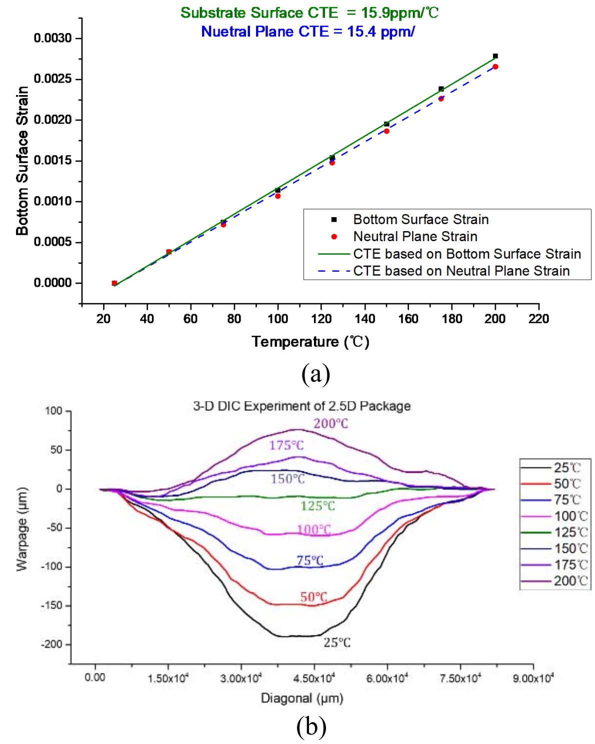

Fig. 14. (a) CTE results on substrate surface and neutral plane. (b) Warpage along the package diagonal on substrate surface.

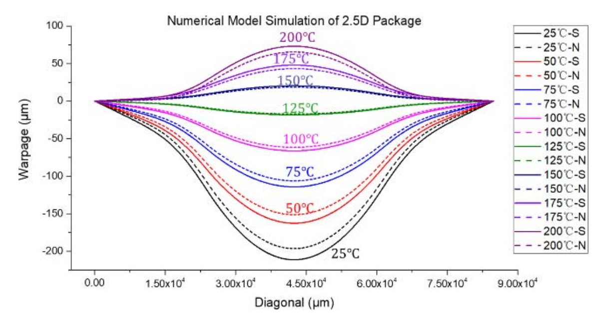

Fig. 15. Warpage plot along the substrate diagonal with surface CTE 15.9 ppm/°C and neutral plane CTE 15.4 ppm/°C.

result [Fig. 14(b)], but the warpage value needs to be further checked. Table V displays the maximum warpage of each case. There is −11.6% bias at room temperature when the bottom surface strain was employed. As the temperature increases to go through the stress-free temperature and approach the reflow temperature, the variance maintains about 10% to 30% difference with the experiment. In this model, the CTE of the substrate is 15.9 ppm/°C, measured from the substrate surface. The 1.8-mm-thick substrate and overall 270-μm warpage affect the determination of thermal strain. Based on this concern, the neutral plane strain was calculated by the method that is introduced in Section III. The model with neutral plane CTE, 15.4 ppm/°C, based on the warpage result of Fig. 14(b), is plotted Fig. 14(a). Then, by keeping other parameters the same, the dashed line of Fig. 14 explicates the warpage behavior with neutral plane CTE. It is clearly observed that new material property tuned the model to be accurate and the

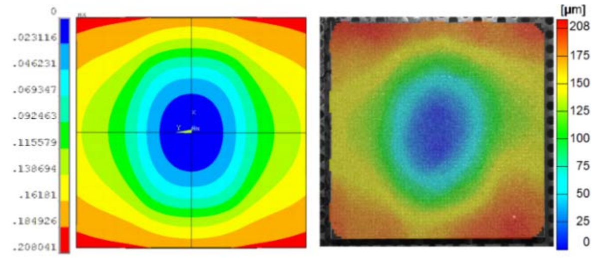

Fig. 16. 2.5-D package warpage at room temperature from numerical model and 3-D DIC.

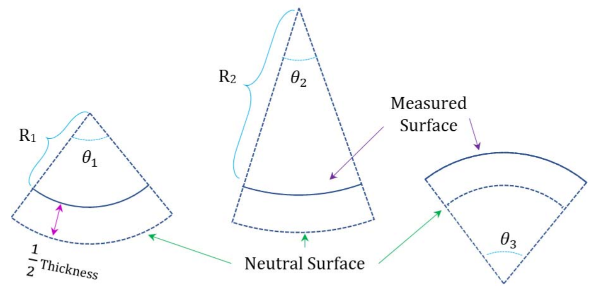

Fig. 17. Schematic of the neutral plane elongation or shrinkage for different warpage situations.

warpage difference as compared to the 3-D DIC is limited in 4% for most of the temperature stages (Table V). When temperature reached 150 °C, the glass transient feature of underfill or molding may mislead the warpage prediction. However, it is no doubt that the neutral plane strain is more cognate to the reality and assists in improving model accuracy.

The case study proves the validity and necessity for the precise determination of material effective strain. The highly verified numerical model (Fig. 16) can play an important role in understanding the effects of material properties and structures to investigate the novel heterogeneous packages and predict the potential failure. The 3-D DIC experiment result helps to accumulate valuable strain information, while the three-point curvature method, which is introduced in this paper, assists in learning the essence of the material strength.

V. Discussion

It is noticed that the neutral plane CTE reduced instead of "compensating" the warpage and thickness effects on strain calculation, but the verification tests always obtained the engineering strain increased on the neutral plane. However, in this case, the maximum substrate warpage of the package occurred at the room temperature, which is treated as the initial reference length to compute the engineering strain. The schematic (Fig. 17) illustrates the situation. Solid curve can be assumed as the 3-D DIC monitoring surface. The left one is the warped surface at room temperature, then the warpage released and even became convex, like the middle and right schematics. To calculate the neutral strain, the length on the neutral plane can be expressed as follows:

$$L_{\text{neutral\_surface\_25 °C}} = \theta_1 \cdot \left(R_1 + \frac{1}{2}t\right)$$
$$L_{\text{neutral\_surface\_75 °C}} = \theta_2 \cdot \left(R_2 + \frac{1}{2}t\right).$$

The elongation of the neutral plane is $\theta_i \cdot (1/2)t$. As the warpage released, the central angle of curvature radius decreased, so that the elongation of neutral plane decreased. After stress-free temperature, the convex warpage even made the neutral plane shorter than the measured surface, as shown in the right schematic of Fig. 17. Then the modified neutral plane strain becomes smaller than the measured surface strain, which means the CTE is smaller as well. On the other hand, when we recall the initial CTE measurement problem at the beginning of Section III, its warpage increased consistently. Then, the neutral plane strain kept increasing.

The designed verification bending tests are based on the rule that it can imitate the warping behavior and the anlytical solution is available. To establish a standard reference of finite-element model, the material properties should be available as well. The regular metal is the best choice because it is simple to access the accurate material properties. The bending load mimicked the thermal load for heterogeneous packages. When the bending beam deflects symmetrically along the z-axis, it is similar to the warpage shape. Also, the pure bending guarantees the stability of the neutral plane without any expansion to complicate the analytical solutions.

VI. Conclusion

This paper introduced the novel 3-D DIC method to perform strain measurement for heterogeneously designed electronic packages or composite materials. The advantage of this method is that it generates the full-field strain without sample size and cross-sectional surface preparation. During the investigation, the out-of-plane deformation is considered when 3-D DIC exports the surface strain.

However, for stereoscopic packages with mixed layers, the thickness and warpage interact together to result in the inaccurate strain result. The three-point common curvature method, based on the subset information of 3-D DIC, was developed and validated analytically and numerically. Its effectiveness was demonstrated by establishing precise finite-element model and predicting the warpage accurately.

As the heterogeneous packages develop, the accurate strain estimation becomes important for learning the deformation and assessing reliability of packages. The 3-D DIC three-point common curvature method satisfies the demands to calculate the neutral plane strain along any direction. The case study reveals the benefits by improving the model and inputting the neutral plane CTE. The wide application 3-D DIC will receive the appreciation of those users for describing the accurate strain on neutral plane and the behavior of heterogeneous electronic packages.

Appendix A

See Fig. 18.

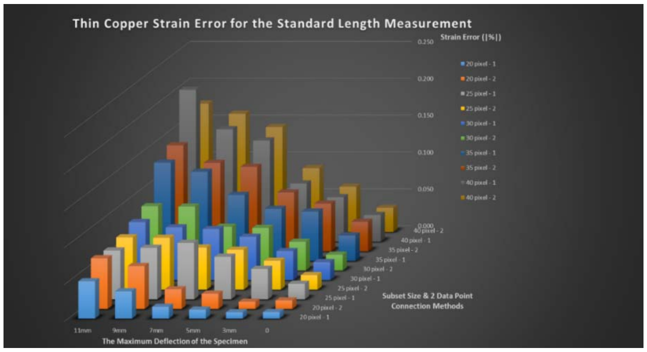

Fig. 18. Strain error for the copper foil with different warping deflections and subset sizes.

Appendix B

$$\begin{aligned}\sigma_x &= -\frac{M\cdot z}{I} = -\frac{(-P)\cdot(x-l)\cdot z}{I}\\ \sigma_z &= 0\\ \tau_{xz} &= \frac{P}{2\cdot I}(t^2-z^2)\\ \varepsilon_x &= \frac{\partial u}{\partial x} = \frac{\sigma_x}{E} = \frac{P\cdot(x-l)\cdot z}{EI} \quad (16)\\ \varepsilon_z &= \frac{\partial w}{\partial z} = -\frac{\nu\cdot\sigma_x}{E} = -\frac{\nu\cdot P\cdot(x-l)\cdot z}{EI} \quad (17)\\ \gamma_{xz} &= \frac{\partial u}{\partial z}+\frac{\partial w}{\partial x} = \frac{\tau_{xz}}{G} = \frac{P}{2GI}(t^2-z^2) \quad (18)\end{aligned}$$

$$(16) \Rightarrow u = \frac{Pz}{2EI}x^2 - \frac{Plz}{EI}x + f(z) \quad (19)$$

$$(17) \Rightarrow w = -\frac{\nu Px}{2EI}z^2 + \frac{\nu Pl}{2EI}z^2 + g(x). \quad (20)$$

From (18)–(20)

$$\frac{Px^2}{2EI} - \frac{Plx}{EI} + f'(z) - \frac{\nu Pz^2}{2EI} + g'(x) = \frac{P}{2GI}(t^2-z^2) \quad (21)$$

$$(21) \Rightarrow \begin{cases} f'(z) = \frac{\nu P}{2EI}z^2 - \frac{P}{2GI}z^2 + e\\ g'(x) = -\frac{P}{2EI}x^2 + \frac{Pl}{EI}x + d \end{cases} \qquad e+d = \frac{Pt^2}{2GI} \quad (22)$$

$$(22) \Rightarrow \begin{cases} f(z) = \frac{\nu P}{6EI}z^3 - \frac{P}{6GI}z^3 + ez + h\\ g(x) = -\frac{P}{6EI}x^3 + \frac{Pl}{2EI}x^2 + dx + i. \end{cases} \quad (23)$$

(19), (20), and (23) $\Rightarrow$

$$\begin{cases} u = \frac{Pz}{2EI}x^2 - \frac{Plz}{EI}x + \frac{\nu P}{6EI}z^3 - \frac{P}{6GI}z^3 + ez + h\\ w = -\frac{\nu Px}{2EI}z^2 + \frac{\nu Pl}{2EI}z^2 - \frac{P}{6EI}x^3 + \frac{Pl}{2EI}x^2 + dx + i. \end{cases} \quad (24)$$

Apply boundary conditions as follows.

1) at $x=0, z=0, u=w=0 \Rightarrow h=i=0$.

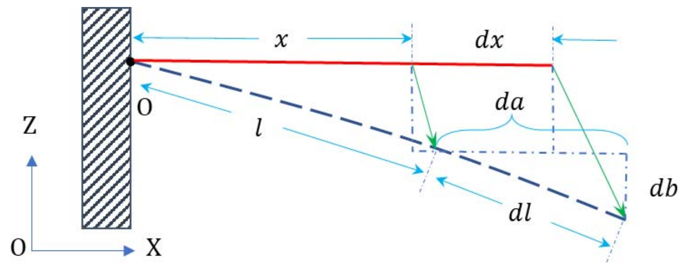

Fig. 19. Schematic of beam length integration.

2) For Timoshenko beam, $(\partial u/\partial z)_{x=0,z=0} = 0$

$$\Rightarrow \left(\frac{Px^2}{2EI} - \frac{Plx}{EI} + \frac{\nu Pz^2}{2EI} - \frac{Pz^2}{2GI} + e\right)_{x=0,z=0} = 0$$
$$\Rightarrow e = 0.$$

Recall $e+d = (\frac{P}{2GI})t^2 \Rightarrow d = (\frac{P}{2GI})t^2$
$\Rightarrow$ (8), and (9).

Apply the geometric information at top and neutral plane
$\Rightarrow$ (10), (11), (12), and (13).

The schematic of Fig. 19 illustrates the relationship between displacement and the total deformed beam length. The red line represents the original length of the beam and the dashed blue line indicates the deformed beam length

$$da = dx + u - u(x) \quad (25)$$
$$db = w(x+dx) - w(x) \quad (26)$$
$$dl = \sqrt{(da)^2 + (db)^2}. \quad (27)$$

Substituting (25) and (26) in (27), we get

$$dl = \sqrt{[dx + u(x+dx) - u(x)]^2 + [w(x+dx) - w(x)]^2}$$
$$\frac{dl}{dx} = \sqrt{\left[1 + \frac{u(x+dx) - u(x)}{dx}\right]^2 + \left[\frac{w(x+dx) - w(x)}{dx}\right]^2}$$
$$\Rightarrow dl = \sqrt{\left[1+\frac{\partial u}{\partial x}\right]^2 + \left[\frac{\partial w}{\partial x}\right]^2}\,dx$$
$$\Rightarrow l = \int_0^l \sqrt{\left[1+\frac{\partial u}{\partial x}\right]^2 + \left[\frac{\partial w}{\partial x}\right]^2}\,dx. \quad (28)$$

For the surface and neutral plane, the displacement (9) to (12) can be utilized to calculate the beam elongation.
$\Rightarrow$ (14) and (15).

References

[1] Y. Niu, J. Wang, and S. B. Park, "The complete packaging reliability studies through one digital image correlation system," in *Proc. IEEE 67th Electron. Compon. Technol. Conf.*, May/Jun. 2017, pp. 1916–1921.
[2] L. Ben Freund and S. Subra, *Thin Film Materials: Stress, Defect Formation and Surface Evolution*. Cambridge, U.K.: Cambridge Univ. Press, 2004.
[3] E. Suhir, "Stresses in Bi-metal thermostats," *ASME J. Appl. Mech.*, vol. 53, no. 3, pp. 657–660, 1986.
[4] E. Suhir, "Interfacial stresses in bimetal thermostats," *ASME J. Appl. Mech.*, vol. 56, no. 3, pp. 595–600, 1989.
[5] P. Chen, P. Raghavan, K. Yazzie, and H. Fei, "On the effective coefficient of thermal expansion (CTE) of bilayer/trilayer in semiconductor package substrates," in *Proc. IEEE 65th Electron. Compon. Technol. Conf.*, May 2015, pp. 1932–1937.

[6] Y. Wen and C. Basaran, "An analytical model for thermal stress analysis of multi-layered microelectronic packaging," *Mech. Mater.*, vol. 36, no. 4, pp. 369–385, 2004.

[7] E. H. Wong, K.-M. Lim, and Y.-W. Mai, "Analytical solutions for PCB assembly subjected to mismatched thermal expansion," *IEEE Trans. Adv. Packag.*, vol. 32, no. 3, pp. 602–611, Aug. 2009.

[8] J.-H. Zhao, Y. Du, M. Morgen, and P. S. Ho, "Simultaneous measurement of Young's modulus, Poisson ratio, and coefficient of thermal expansion of thin films on substrates," *J. Appl. Phys.*, vol. 87, no. 3, pp. 1575–1577, 2000.

[9] C. Basaran and Y. Zhao, "Mesh sensitivity and FEA for multi-layered electronic packaging," *J. Electron. Packag.*, vol. 123, no. 3, pp. 218–224, 2001.

[10] W. Fang and C.-Y. Lo, "On the thermal expansion coefficients of thin films," *Sens. Actuators A, Phys.*, vol. 84, no. 3, pp. 310–314, 2000.

[11] B. Cunningham, R. Weese, P. Lewis, P. Harwood, and T. Tran, "CTE and ratchet growth measurements on LX17-1 and constituents," in *Proc. 24th Aging, Compat. Stockpile Stewardship Conf.*, 2002, pp. 1–7.

[12] B. Han and Y. Guo, "Determination of an effective coefficient of thermal expansion of electronic packaging components: A whole-field approach," *IEEE Trans. Compon., Packag., Manuf. Technol. A*, vol. 19, no. 2, pp. 240–247, Jun. 1996.

[13] Y. Zhao, C. Basaran, A. Cartwright, and T. Dishongh, "Thermomechanical behavior of micron scale solder joints under dynamic loads," *Mech. Mater.*, vol. 32, no. 3, pp. 161–173, 2000.

[14] A. F. Bastawros and A. S. Voloshin, "Transient thermal strain measurements in electronic packages," *IEEE Trans. Compon., Hybrids, Manuf. Technol.*, vol. 13, no. 4, pp. 961–966, Dec. 1990.

[15] B. J. Cunningham, F. J. Gagliardi, and L. Ferranti, Jr., "Low strain rate measurements on explosives using DIC," in *Proc. SEM Annu. Conf. Expo. Experim. Appl. Mech.*, 2010, pp. 1–7.

[16] Y. Niu, H. Wang, S. Shao, and S. B. Park, "In-situ warpage characterization of BGA packages with solder balls attached during reflow with 3D digital image correlation (DIC)," in *Proc. IEEE 66th Electron. Compon. Technol. Conf.*, May/Jun. 2016, pp. 782–788.

[17] M. Sutton, W. J. Wolters, W. Peters, W. F. Ranson, and S. R. McNeill, "Determination of displacements using an improved digital correlation method," *Image Vis. Comput.*, vol. 1, no. 3, pp. 133–139, Aug. 1983.

[18] M. A. Sutton, C. Mingqi, W. H. Peters, Y. J. Chao, and S. R. McNeill, "Application of an optimized digital correlation method to planar deformation analysis," *Image Vis. Comput.*, vol. 4, no. 3, pp. 143–150, 1986.

[19] Y. Niu, H. Lee, and S. Park, "A new in-situ warpage measurement of a wafer with speckle-free digital image correlation (DIC) method," in *Proc. IEEE 65th Electron. Compon. Technol. Conf.*, May 2015, pp. 425–431.

[20] Y. Niu, S. Shao, S. B. Park, and C.-L. Kao, "A novel speckle-free digital image correlation method for *in situ* warpage characterization," *IEEE Trans. Compon., Packag., Manuf. Technol.*, vol. 7, no. 2, pp. 276–284, Feb. 2017.

[21] M. A. Sutton, J. H. Yan, V. Tiwari, H. W. Schreier, and J. J. Orteu, "The effect of out-of-plane motion on 2D and 3D digital image correlation measurements," *Opt. Lasers Eng.*, vol. 46, no. 10, pp. 746–757, 2008.

[22] O. De Almeida, F. Lagattu, and J. Brillaud, "Analysis by a 3D DIC technique of volumetric deformation gradients: Application to polypropylene/EPR/talc composites," *Compos. A, Appl. Sci. Manuf.*, vol. 39, no. 8, pp. 1210–1217, 2008.

[23] S. Timoshenko, "Deflection of beams," in *Strength of Materials*, 3rd ed. Malabar, FL, USA: Kriger, 1976, pp. 137–175.

[24] M. A. Sutton, S. R. McNeill, J. D. Helm, and Y. J. Chao, "Advances in two-dimensional and three-dimensional computer vision," in *Photomechanics*, vol. 77. Berlin, Germany: Springer, 2000, pp. 323–372.

[25] C. Lane, R. L. Burguete, and A. Shterenlikht, "An objective criterion for the selection of an optimum DIC pattern and subset size," in *Proc. 6th Int. Congr. Expo.*, 2008, pp. 1–9.

[26] Y. Niu, H. Wang, and S. B. Park, "A general strategy of in-situ warpage characterization for solder attached packages with digital image correlation method," *Opt. Lasers Eng.*, vol. 93, pp. 9–18, Jun. 2017.

[27] G. M. Hassan, C. MacNish, A. Dyskin, and I. Shufrin, "Digital image correlation with dynamic subset selection," *Opt. Lasers Eng.*, vol. 84, pp. 1–9, Sep. 2016.

[28] S. Timoshenko, "Two-dimensional problems," in *Theory of Elasticity*, 1st ed. York, PA, USA: Maple Press, 1934, pp. 27–51.

[29] S. Timoshenko, "Elastic curve," in *History of Strength of Materials*. York, PA, USA: Maple Press, 1953, pp. 25–41.

[30] M. H. Sadd, "Strain energy and related principles," in *Elasticity: Theory, Applications, and Numerics*. Burlington, MA, USA: Academic, 2009, pp. 113–133.

Yuling Niu, photograph and biography not available at the time of publication.

Van-Lai Pham, photograph and biography not available at the time of publication.

Jing Wang, photograph and biography not available at the time of publication.

Seungbae Park, photograph and biography not available at the time of publication.